An optimal XBT-based monitoring system for the South Atlantic Meridional Overturning Circulation at 34°S

Marlos Goes,[1,2] Gustavo Goni,[2], and Shenfu Dong[1,2]

Corresponding author: Marlos Goes, CIMAS/University of Miami and NOAA/AOML, Miami, USA. (marlos.goes@noaa.gov)

[1]CIMAS, University of Miami, Miami, FL, USA.

[2]PHOD, NOAA/AOML, Miami, FL, USA.

Abstract. The South Atlantic is an important pathway for the inter-basin exchanges of heat and freshwater with strong influence on the global meridional overturning stability and variability. Along the 34°S parallel, a quarterly, high resolution XBT transect (AX18) samples the temperature structure in the upper ocean. The AX18 transect has been shown to be a useful component of a meridional overturning monitoring system of the region. However, a feasible, cost-effective design for an XBT-based system has not yet been developed. Here we use a high-resolution ocean assimilation product to simulate an XBT-based observational system across the South Atlantic. The sensitivity of the meridional heat transport, meridional overturning circulation, and geostrophic velocities to key observational and methodological assumptions is studied. Key assumptions taken into account are horizontal and temporal sampling of the transect, salinity and deep temperature inference, as well as the level of reference for geostrophic velocities. With the current sampling strategy, the largest errors in the meridional overturning and heat transport estimations are the reference velocity for geostrophic calculations and the western boundary resolution. We use the results obtained by the state estimation under observational assumptions to make recommendations for potential improvements in the AX18 transect implementation.

1. Introduction

The Atlantic Ocean circulation is well known for having a deep convection site at high latitudes in the northern hemisphere, which drives to a large extent the Atlantic meridional overturning circulation (AMOC) and, therefore, the northward heat transport to the northern latitudes [*Marshall and Schott*, 1999]. The variability of the AMOC is partly responsible for changes in the northern hemisphere climate, such as the North Atlantic storm tracks [*Woollings et al.*, 2012] and the North American and European precipitation patterns [*Enfield et al.*, 2001; *Sutton and Hodson*, 2005], sea level variability [*Levermann et al.*, 2005; *Hu et al.*, 2011], uptake of ocean tracers such as CO_2 [*Sabine et al.*, 2004; *Goes et al.*, 2010], tropical precipitation [*Zhang and Delworth*, 2006] and El Niño patterns [*Dong and Sutton*, 2007; *Timmermann et al.*, 2007].

Despite the fact that the AMOC strength and variability are highly determined by changes within the North Atlantic Subpolar gyre [*Hatun et al.*, 2005; *Lohmann et al.*, 2009], the deep convection regions between the Greenland-Iceland-Scotland seas are highly sensitive to heat and freshwater transported from the South Atlantic [*Rahmstorf*, 1996; *Donners and Drijfhout*, 2004], which is suggested to be one of the main drivers of two stable states of the AMOC [*Weijer et al.*, 1999; *Beal et al.*, 2011; *Hawkings et al.*, 2011; *Garzoli et al.*, 2013].

The South Atlantic is an important pathway for exchange of heat and water masses from other basins through, for example, the Agulhas current region [*Goni et al.*, 1997] and the Brazil-Malvinas Confluence region [*Gordon*, 1986; *Wainer et al.*, 2000; *Goni and Wainer*, 2001; *Lentini et al.*, 2006; *Goni et al.*, 2011]. The South Atlantic Ocean has been historically one of the least observed regions on the globe; however, several efforts to measure long-term variability in the basin have been put forward in the last decade. For instance, expendable bathythermograph (XBT) observations from the High-Density XBT transect AX18 (Figure 1a) obtain temperature section in the upper 800 m of the ocean four times a year along 34°S. Studies based on the AX18 XBT data have shown that the mean strength of AMOC and heat transport at 34°S are mostly geostrophically driven, although the seasonal variability of the meridional transports are equally determined by the geostrophic and the wind-driven Ekman components [*Dong et al.*, 2009]. The compensation between the Ekman and geostrophic components may translate into a small annual cycle of heat and volume transports [*Garzoli and Baringer*, 2007; *Dong et al.*, 2009], although models generally do not reproduce this characteristic [*Dong et al.*, 2011a].

Currently, observational estimates rely on several assumptions to estimate the integral flow in the South Atlantic. Thus far, only *Baringer and Garzoli* [2007] have estimated some of the uncertainty resulting from the underlying XBT-based observational system methodological assumptions to measure heat transport across 34°S. However, no sensitivity tests have yet been performed to derive an optimal AX18 sampling strategy, i.e., a feasible strategy that maximizes the information content in a cost-effective manner, and to assess the uncertainty in volume and heat transports associated with observational and computational methodologies across 34°S. To accomplish this, current high resolution ocean reanalyses can be useful to assess and investigate potential improvements in the sampling strategy of the AX18 transect. Similar methodologies have been applied, for example, in several studies in the North Atlantic [e.g. *Hirschi et al.*, 2003; *Baehr et al.*, 2004, 2008] to evaluate strategies for monitoring the MOC in the North Alantic.

The goals of the present study is to assess how observational and computational methodologies affect the estimates of volume and heat transports across 34°S in Atlantic Ocean, and to help improve the design of the AX18 XBT transect in order to reduce uncertainty in its estimates. Therefore, this study will address four main objectives to reach these goals:

i) The optimal spatial (longitudinal) resolution along the AX18;

ii) The optimal temporal sampling to capture the seasonal variability of the AMOC in the region;

iii) The uncertainties derived from the salinity and deep temperature estimation;

iv) Potential improvements to the assumptions made regarding the level of reference to resolve the barotropic mode.

To address these objectives, we will first describe the characteristics of the region of study (Section 2). We will describe the high-resolution global assimilation model (Section 3) used in this study. We will define the methodology (Section 4) to calculate volume and meridional heat transport (MHT) across 34°S, and perform controlled experiments in the model framework to answer point-by-point the above questions (Section 5). Finally, we will discuss the results and make recommendations for the improvement of the AX18 XBT transect measurements (Section 6).

2. Regional characteristics

The subtropical South Atlantic is characterized by a large scale anticyclonic feature, the South Atlantic subtropical gyre [*Stramma and England*, 1999; *Garzoli and Matano*, 2011]. In the southwestern Atlantic, the surface dynamics are dominated by the Brazil-Malvinas Confluence, which is characterized by the cold northward flow of the Malvinas Current, and a southward flowing warm weak western boundary current, the Brazil Current [*Garzoli*, 1993]. This region exhibits complex frontal motions [*Goni et al.*, 2011; *Goni and Wainer*, 2001] and patterns with the simultaneous presence of warm and cold rings and eddies [*Lentini et al.*, 2006] and, therefore, it is characterized by large values of eddy kinetic energy (Figure 1a). In the southeastern Atlantic, the transfer of warm waters from the Indian Ocean into the South Atlantic subtropical gyre largely takes place in the form of rings and filaments formed when the Agulhas Current retroflects south of Africa between 1°W and 25°E [*Richardson and Garzoli*, 2003; *Goni et al.*, 1997]. The eastward flowing South Atlantic Current and the northward flowing Benguela Current delimit the southern and eastern boundaries of the subtropical gyre, respectively. The Brazil-Malvinas Confluence region and the Agulhas retroflection region represent the most energetic areas contained in the South Atlantic. These two regions present similar values of mean eddy kinetic energy, above 1000 cm^2 s^{-2} (Figure 1a), as revealed by altimetric sea level anomalies [*Ducet et al.*, 2000] for the 2007-2012 time period. The Brazil-Malvinas Confluence and Agulhas retroflection regions are both crossed by the XBT transect AX18 (Figure 1a).

3. The HYCOM-NCODA reanalysis

As suggested in previous studies, the strong mesoscale energy in the South Atlantic region requires a minimum of eddy-permitting models to resolve its main features [*Treguier et al.*, 2007; *Biastoch et al.*, 2009]. In the present study we use data from the Hybrid Coordinate Ocean Model (HYCOM)-Navy Coupled Ocean Data Assimilation (NCODA) assimilative product [*Chassignet et al.*, 2009], which has been previously applied in several studies in the South Atlantic [*Mello et al.*, 2013]. We use a total of nearly 6 years of model simulation, from June 2007 to May 2013, sampled in a 7-day timestep using 7-day averages.

The HYCOM-NCODA is configured for the global ocean with HYCOM 2.2 as the dynamical model. Computations are carried out on a Mercator grid between 78°S and 47°N, with an average of 1/12° ($\sim$ 7 km) horizontal spacing and 32 vertical layers. A bipolar patch is used for regions north of 47°N. Bathymetry is derived from the U. S. Naval Research Laboratory 2-minute DBDB2 (Digital Bathymetric Data Base) dataset. Surface forcing is from the Navy Operational Global Atmospheric Prediction System (NOGAPS) and includes 3-hourly and 0.5° wind stress, wind speed, heat flux (using bulk formula), and precipitation. The NCODA methodology [*Cummings*, 2005] uses the model forecast as a first guess in a multi-variate Optimal Interpolation (MVOI) scheme and assimilates available along-track satellite sea height anomaly observations (obtained via the Naval Oceanographic Office's Altimeter Data Fusion Center), in-situ sea surface temperature (SST), as well as available in-situ vertical temperature and salinity profiles from XBTs, ARGO floats, and moored buoys. The Modular Ocean Data Assimilation System (MODAS) synthetic profiles are used by NCODA for downward projection of surface information [*Fox et al.*, 2002].

Compared to altimetric observations, the eddy-resolving HYCOM-NCODA reanalysis reproduces reasonably the main circulation features of the region (Figure 1b). The output of this model, however, shows lower energy in the high EKE regions, such as the Brazil-Malvinas Confluence and Agulhas retroflection regions, and higher energy in the low EKE regions (Figure 1c). The negative energy biases are also observed in the comparison of the sea level root-mean square variability of the AX18 transect boundaries (Figure 2a, b, c). We select 18 realizations (Figure 2a) of the AX18 transect based on the criteria of being zonally directed (median angle $< 10°$, and with the mean section between 30° and 36° of latitude) to compare the model thermohaline behavior with the actual XBT observations along the nominal 34°S. Below 850 m, the maximum depth sampled by the XBTs, the WOA05 annual climatology [*Locarnini et al.*, 2006] is used. The mean temperature section retrieved by the AX18 along the nominal of 34°S shows an east-west gradient, with higher upper ocean temperatures in the west (Figure 2d). The associated zonal density gradients allow average geostrophic volume and heat transports to the north, as shown in previous studies [e.g., *Ganachaud and Wunsch*, 2003; *Garzoli and Baringer*, 2007]. The model shows generally negative temperature biases in the interior (1 to 2°C on average), which indicates stronger stratification and and shoaling of isothermal layers, and positive biases on the boundaries (1 to 1.5 °C on average) relative to the mean AX18 section above 850 m, and stronger ocean bottom stratification in comparison to the WOA05 climatology (Figure 2g–i).

4. Methodology

This study focuses on the reconstruction of the AMOC streamfunction (Ψ_y) and the heat transport (MHT) along 34°S by simulating XBT observations in the model framework. For this, we use the temperature, salinity and velocity outputs of the model, distributed over depth and longitude along the 34°S. This section describes how the AMOC and MHT are defined through the paper.

4.1. AMOC

The AMOC streamfunction is defined as:

$$\Psi_y(z) = \int_{x_E}^{x_W} \int_{z}^{-H} v(x,z)\, dxdz\,, \tag{1}$$

i.e., the integral of the meridional velocity $v(x,z)$ from the bottom (H) to the depth (z) of the ocean and between the western (x_W) and the eastern (x_E) boundaries of the basin. The meridional velocity $v(x,z)$, and therefore its derived meridional streamfunction, can be decomposed into three dynamical components [*Lee and Marotzke*, 1998]:

$$v(x,z) = v_{sh}(x,z) + v_{bar}(x) + v_E(x,z), \tag{2}$$

where v_{sh} is the vertical shear component, which consists of the velocities calculated using the thermal wind relationship, minus a depth independent velocity:

$$v_{sh}(x,z) = \frac{g}{\rho_0 f}\frac{\partial \rho}{\partial x} - \frac{1}{H}\int_{-H}^{0} v_{sh}(x,z)\, dz, \tag{3}$$

where $\rho_0 = 1025$ kg m^{-3} is the mean water density, f is the Coriolis parameter, and g is the local gravity. The depth independent velocity is known as the barotropic or gyre component v_{bar}, and is here defined as the local average of $v(x,z)$ over the depth H of the ocean:

$$v_{bar}(x) = \frac{1}{H}\int_{-H}^{0} v(x,z)\, dz, \tag{4}$$

and the last term $v_E(x,z)$ is the Ekman component, derived from the local zonal wind stress (τ_x), compensated by a depth-independent flow underneath the Ekman layer:

$$v_E = -\frac{\tau_x}{\rho_0 f D_E} - \frac{1}{H}\int_{-H}^{0} v_E(x,z)\, dz, \tag{5}$$

where D_E is the depth of the Ekman layer, which is arbitrarily assumed here to be D_E = 50 m [e.g., *Pond and Pickard*, 1983]. Therefore the Ekman velocity assumes only two different values in the water column, one in the Ekman layer, and another below the

Ekman layer [*Baehr et al.*, 2004]. Other ageostrophic contributions rather than Ekman (frictional and non-linear) are not defined. The barotropic and vertical shear velocities combined constitute the absolute geostrophic velocity, which is estimated using the dynamic method assuming a reference level [*Pond and Pickard*, 1983]. Barotropic velocities have a strong contribution to the geostrophic flow at locations of sloping topography, and their projection on the AMOC can therefore be an important term in the AMOC reconstruction [*Baehr et al.*, 2004]. To ensure zero mass transport, a correction is applied to the three components of the meridional velocity by subtracting a spatially constant term proportional to the weighted mean velocity accross the section:

$$v(x,z) = v(x,z) - \frac{M_y}{\int_{-H}^{0}\int_{x_E}^{x_W} dxdz}, \qquad for\ M_y = \int_{-H}^{0}\int_{x_E}^{x_W} v(x,z)\, dxdz \tag{6}$$

The AMOC strength (in Sv) is further defined as the value of the maximum amplitude of the AMOC streamfunction (Equation 1). Since the total velocity is decomposed into its phisical components in Equation 2, an AMOC strength can also be defined for the individual components of the AMOC.

4.2. Meridional Heat Transport

The meridional heat transport is calculated as follows:

$$MHT = \rho_0 c_p \int_{-H}^{0}\int_{x_E}^{x_W} v(x,z)\theta(x,z)\, dxdz - \rho_0 c_p M_y \langle\theta\rangle, \tag{7}$$

where $c_p = 4187$ J kg^{-1}K^{-1} is the specific heat of sea water, and $\langle\theta\rangle$ is the averaged potential temperature θ along the section. The last term in Equation 7 is a constraint to allow zero mass transport across the section, which is necessary for heat transport calculations in free surface models, since they do not necessarily have zero mass transport at any given time period [*Jayne and Marotzke*, 2001; *Griffies et al.*, 2004].

To reconstruct the MHT, Equation 7 is further decomposed into the same components as the meridional overturning, i.e., vertical shear, barotropic and Ekman, respectively, using the corresponding decomposition of the velocity (Equation 2). Following *Hall and Bryden* [1982]:

$$MHT = \rho_0 c_p \int_{-H}^{0} \int_{x_E}^{x_W} \{v_{vs}[\theta - \theta_{bar}] + v_{bar}\theta_{bar} + v_{Ek}\theta_{Ek}\} dx dz \tag{8}$$

where θ_{bar} is the depth-averaged potential temperature, and θ_{ek} follows the Ekman velocity definition, i.e., θ_{ek} assumes only two values over depth, one as the average in the Ekman layer, and another in the layer below the Ekman layer. Each of the terms in Equation 8 is meaningful as a heat transport, because the velocity components are designed to be compensated and allow zero net volume transport across the section [*Hirschi et al.*, 2003]. Therefore, in the reconstruction, the last term in Equation 7 is not necessary. Otherwise, the calculated heat transport would be dependent on an arbitrary temperature reference [*Montgomery*, 1974].

5. Results

5.1. AMOC streamfunction reconstruction

The AMOC strength calculated from the model output velocities in a 7-day average is highly variable in time (Figure 3a; black line), with amplitude ranging from -5 to 35 Sv (1 Sv = 10^6 m^{3}s^{-1}), and with strong high frequency variability as well as a defined annual cycle. The time-averaged AMOC streamfunction (Figure 3c) shows positive (northward) values in the upper 3500 m, negative (southward) values underneath, and a pronounced maximum at the depth of $\sim$ 1500 m, which characterizes the AMOC strength. The time-mean AMOC strength in the model is 15.1 $\pm$ 6.8 Sv, lower than observational estimates of 17.9 ± 2.2 Sv [*Dong et al.*, 2009], but within the uncertainty estimates. Results from other high resolution models, e.g. [*Dong et al.*, 2011a] using the OFES model, show a strong agreement with the AMOC strength value (15.0 ± 3.7 Sv) presented here.

We decompose the AMOC streamfunction into its vertical shear, Ekman, and barotropic components using the methodology described in Section 4.1. Therefore, each component is independently estimated, accordingly to *Lee and Marotzke* [1998] and *Baehr et al.* [2004], but differently from the methodologies of *Perez et al.* [2011] and *Dong et al.* [2011a], which estimate the geostrophic transport either unbalanced for mass transport or as the residual between the total and Ekman transports. The absolute geostrophic component (barotropic plus vertical shear) is calculated using a level of known motion at the bottom of the ocean, assuming that velocities are perfectly known there. Individually, the vertical shear component has the strongest contribution to the mean AMOC strength (Figure 3b), with an average of 26.9 ± 3.6 Sv, and it is in great part compensated by the barotropic contribution of the transport, which is negative (southward) with an average of -16.3 ± 6.3 Sv. The resulting absolute geostrophic transport is 12.6 ± 3.2 Sv, smaller than the observational value of 15.7 ± 2.6 Sv [*Dong et al.*, 2009], but similar to that obtained from the OFES model (12.9 ± 2.1 Sv; *Dong et al.* [2011a]). It is worth mentioning that neither the barotropic nor the vertical shear streamfunctions show a reversal in depth, as observed on the total mean streamfunction, but that the addition of these two streamfunctions produces the same reversal pattern at approximately 3500 m (magenta line in Figure 3c) as observed in the original model streamfunction. Strong interannual variability is observed in the barotropic component, with positive anomalies in the austral summer of 2007 and 2008 and negative anomalies in the austral spring of 2009 and 2010. The Ekman component has the lowest contribution to the mean AMOC strength, only 2.0 ± 4.0 Sv, but its maximum amplitude (variability) can reach over 10 Sv, which is stronger than the other components.

The MHT follows the same pattern as the AMOC (Figure 4). The mean MHT calculated directly from the model fields is 0.33 ± 0.5 PW (1 PetaWatt = 10^{15}W), which is also lower than the values calculated from observational studies (0.54 ± 0.14 PW; *Garzoli et al.* [2013]). The barotropic MHT component (-0.60 ± 0.23 PW) compensates to a large extent the vertical shear component (0.81 ± 0.35 PW), and the Ekman component contributes about one third of the total MHT (0.12 ± 0.24 PW).

The annual variability of the AMOC and MHT components (Figure 5) shows that the vertical shear component does not have a noticeable annual cycle. The Ekman and barotropic components have stronger annual cycles, and are approximately in phase with each other, with more positive/less negative values from March to August. Therefore, the total geostrophic transport (vertical shear plus barotropic) and the Ekman components have similar phases, a result that differs from previous observational studies [e.g., *Dong et al.*, 2009] that show an out-of-phase relationship between the Ekman and geostrophic AMOC annual cycle, which produces a much reduced annual cycle of the AMOC variability. However, other high-resolution models also show a similar annual cycle for the total AMOC [e.g., *Dong et al.*, 2011a; *Perez et al.*, 2011] as observed here. The residual contribution, which is the part of the annual variance that is not explained by the reconstruction (cyan line, Figure 5), is negligible for the AMOC but can reach up to -0.2 PW for the MHT, especially during the austral summer. As observed in Figure 4a, the MHT calculated directly from the model velocities is weak or sometimes negative during austral summer, but these reversals of MHT are hardly featured in the reconstruction (Figure 4a, magenta line). Consequently, the reconstruction produces a higher mean MHT of 0.39 ± 0.36 PW. These differences may arise because the model velocities contain ageostrophic terms other than Ekman [*Sime et al.*, 2006], non-linearities in the MHT calculation, and unbalanced flow of volume (0.94 ± 3.8 Sv), whose MHT contribution is here estimated at -0.02 ± 0.06 PW (Equation 8), the same mean magnitude of 0.02 PW estimated in *Baringer and Garzoli* [2007].

5.2. XBT observational strategy

The AX18 XBT transect, which was designed with the main purpose of monitoring the variability of the upper limb of the AMOC transport, measures temperature sections in the upper ocean between Cape Town and South America quarterly, with a high-density (between 25-50 km) zonal spacing.

Observational studies that used AX18 data to estimate meridional volume and heat transports involved several methodological assumptions. The XBTs measure temperature profiles in the upper 800 m depth (e.g. Deep Blue probe type). Because XBTs do not measure salinity, a common method to infer salinity profiles at an XBT deployment location uses a lookup table derived from historical temperature-salinity (T-S) relationships [*Thacker*, 2008]. Below 800 m, the temperature and salinity profiles are extended down to the bottom of the ocean with their climatological values [*Baringer and Garzoli*, 2007; *Dong et al.*, 2009]. The barotropic or external mode is generally estimated by adopting a level of no motion at the depth where the potential density anomaly referenced to 2000 dbar assumes the value of 37.09 Kg m^{-3} (σ_2 = 37.09) [*Ganachaud and Wunsch*, 2003; *Baringer and Garzoli*, 2007]. The σ_2 = 37.09 depth is approximately located at

3700 m depth and between two water masses, the North Atlantic Deep Water (NADW) flowing southward between 1500 and 3700 m, and the underlying Antarctic Bottom Water (AABW) flowing northward [*Ganachaud and Wunsch*, 2003]. The Ekman component of the flow is calculated from available zonal wind stress products at the XBT deployment locations.

In order to simulate the XBT observations in the model, we make the same assumptions as used in the observational studies: i) the model temperature data are used above 800 m, ii) a quadratic least squares fit between the annual mean temperature and salinity obtained from the model is specified for each depth, calculated using 1 degree boxes along 34°S, iii) the monthly climatology of temperature and salinity at a 1 degree longitudinal resolution is padded below 800 m to extend the pseudo-observations to the bottom of the ocean, and iv) a reference level for the geostrophic velocity calculation is chosen. Constructing the T-S relationships from the model instead of using, for example, the World Ocean Atlas (WOA) climatology is necessary, since the model's own internal biases relative to the observations could potentially bring spurious T-S discontinuities. The WOA climatology is subject to biases in regional coverage, such as below 2000 m (the parking depth of Argo floats), along coastal areas, and historically in the South Atlantic. Here, we do not account for imperfect sampling although its effects can be sizeable in producing additional seasonal biases.

The RMS error between the model salinity and the salinity estimated from the lookup table is shown in Figure 6. In the top 200 m, salinity errors are on the order of 0.1 psu. Higher differences (~ 0.4 psu) are found in the western side of the basin in the upper 100 m, where there is a fresh water inflow from river runoff. Below 200 m the RMS difference is generally lower than 0.1 psu, with higher values located around 500 m and decreasing to near zero below 1000 m. These error values are on the same order of magnitude of the RMS of the salinity annual cycle and, therefore, are highly driven by the seasonal variation of T-S relationships, which is not captured by the annual mean T-S relationships.

5.3. AMOC and MHT uncertainties due to the XBT transect observational sampling

In this section we investigate the meridional transport uncertainties associated with the observational sampling. We will explore two main sources of uncertainty, that relate to: i) the temporal resolution and ii) the horizontal resolution. We apply each of the two assumptions individually in order to quantify their uncertainties, which will allow recommending improvements in the AX18 transect design and implementation.

5.3.1. Temporal resolution

The AX18 transect was originally implemented to be carried out four times a year, and estimates of the geostrophic AMOC transport can only be performed at the time of each AX18 transect realization. The rate of time sampling as well as the year-to-year variability of number of transects may alias the estimates of the annual cycle of the AMOC and meridional heat transport [*Bryden et al.*, 2005]. We simulate in the model uncertainties associated with the transect temporal sampling by randomly selecting points in the timeseries of the geostrophic AMOC and MHT, and use the RMS difference of monthly means of these two quantities as a measure of the uncertainty associated with the temporal sampling. We vary two parameters associated with the temporal sampling of the AX18 transect: The number of realizations per year, from 1 to 20 times per year, and the number of years of data collection, from 1 to 15 years. The random sampling is calculated in three steps. First the original timeseries of the AMOC and MHT are extented by padding up to 100 years. Some small stochastic noise is added to the extended timeseries. Seasonality is maintained in this timeseries by choosing accordingly the beginning of each padded timeseries. Second, a stretch of the 100-year timeseries is chosen with its length defined by the uncertain parameter number of years sampled. Third, according the number of samples per year, random samples are taken from the stretch of the time series. In this step the samples are evenly distributed around the year, for example, with a two sample per year parameter setting, one sample is taken every semester. These steps are reproduced 400 times, which is a number sufficiently high to allow all months to be sampled and the average of all realizations to have the same monthly means as the original model geostrophic AMOC and MHT. Furthermore, the mean monthly RMS difference of the 400 realizations will define a measure of the uncertainty associated with the time sampling. Contour plots showing the sampling error variability of the AMOC and MHT with respect to the number of years measured and the number of samples per year is shown in Figure 7. The time sampling error of the AMOC and MHT show similar behavior, i.e., errors decrease exponentially as more samples are collected during the year or when a higher number of years is sampled. The RMS errors are as low as 0.5 Sv and 0.05 PW when carrying out up to 12 transect realizations per year for 15 years. On the other hand, when transects are carried out twice a year for two years, the errors are above 2.5 Sv and 0.25 PW, respectively. The current number of realizations of the AX18 transect along the nominal of 34°S is 18 (Figure 2), which are done approximately on a quarterly basis. This is equivalent to a total sampling period of five years in our considered parameter space. Therefore, according to our model estimates, the associated RMS errors of the AMOC and MHT are 2.3 Sv and 0.23 PW, respectively (stars in Figure 7), close to the most uncertain values in the studies parameter space. Although 12 realizations per year is difficult to achieve operationally, current discussions for increasing the number of transect realizations to five or six per year are underway. This would lower the RMS errors to < 2.0 Sv for the AMOC and < 0.20 PW for the MHT, which may allow a greater improvement over the years.

One additional temporal sampling error arises from the non-synopticity of the XBT transect measurements. An AX18 realization takes approximately 10 days to complete the trajectory from South America to Cape Town, which may alias the transport estimates across this transect. We quantify here the errors due to non-synopticity by simulating the same observational assumptions within the model environment. In this experiment, we simulate one AX18 XBT realization for each model day by using 10 bins of meridional velocity values from east to west that correspond to 10 consecutive days of model velocity. The AMOC and MHT are estimated every 7 days from these simulations, using as the time tag the first day of each non-synoptic field. These estimates are compared against the ones from the synoptic model outputs.The errors associated with the non-synopticity of the data for the whole period of the simulation are 0.21 ± 4.1 Sv for the AMOC and 0.01 ± 0.25 PW for MHT. The RMS values due to non-synopticity are on the same order as the RMS errors produced by the quarterly sampling. However, since this calculation is performed over model daily values instead of 7-day averages, these RMS values are actually an overestimation in comparision to the other experiments.

5.3.2. Horizontal sampling

The AX18 XBT transect crosses three regions of different dynamic regimes (Figure 1): i) the western (Confluence region), interior (gyre), and eastern (Agulhas leakage) regions. Previous studies suggest that it is critical to account for the variability in all three regions in order to monitor and quantify changes in the AMOC and MHT [*Dong et al.*, 2009]. The current XBT spatial sampling strategy accounts for the different regional characteristics: at a lower density ($\sim$ 50 km) in the interior region, and at higher density ($\sim$ 25 km) closer to the boundaries, i.e., east of the Walvis Ridge ($\sim$ 1°W) and west of 40°W, outside the continental slope region in South America. This sampling strategy is a heuristic approach to add more spatial resolution to the high energy boundary regions (Figure 1). Here we quantify the sensitivity of the meridional transport changes to the horizontal sampling in these three regions. To accomplish this, we generate an ensemble with 30 members by degrading the longitudinal resolution in each of the three regions at a time, from the original 0.08 degree ($\sim$ 7.3 km) model grid up to 5 degrees ($\sim$ 460 km) at variable steps, giving more emphasis to the high resolution sampling. We use the RMS error, bias, and correlation as metrics to compare the reconstructions to the original AMOC and MHT strength.

Our results show that the AMOC strength and MHT are less sensitive to changes in the spatial resolution in the interior than at the boundary regions (Figure 8). For the AMOC, degrading the resolution in the interior to a 3° degree longitude sampling produces a small negative bias and RMS error of -0.45 $\pm$ 1.3 Sv, and a minimum correlation of $\sim$ 0.9. For a 50 km resolution ($\sim$ 0.6°), the error is -0.1 $\pm$ 1.1 Sv and 0.01 $\pm$ 0.06 PW. In the boundary regions, the AMOC and MHT are more sensitive to changes in spatial sampling. The bias and RMS error for a 25 km ($\sim$ 0.3°) spacing is of 1.7 $\pm$ 2.4 Sv/0.03 $\pm$ 0.06 PW in the western and 1.0 ± 1.4 Sv/-0.03 ± 0.04 PW in the eastern boundary. The correlation is about 0.9 at 25 km spacing in the boundaries, and decreases to 0.6 when longitudinal sampling is larger than ∼ 90 km (1°). The larger decrease of correlation in the boundaries is partly due to subsampling of strong currents and high mesoscale activity, and also because the shelf transport may not be observed at lower sampling rates. The potentially unresolved volume transports in the continental shelves (above 200 m deep) are -0.61 ± 0.77 Sv in the west and 0.15 ± 0.44 Sv in the east of the basin. Both transports on the shelf contribute only a negligible temperature transport ($\sim 10^{-8}$ PW), which agrees with the estimates of *Baringer and Garzoli* [2007]. Therefore, a higher AX18 horizontal sampling is indeed needed in the eastern and western boundaries, especially in the western side of the basin, where the current sampling biases are larger in comparison to the other regions.

Interestingly, biases in the MHT have opposite signs and similar magnitudes when comparing the western and eastern boundaries for any given zonal sampling resolution (Figure 8c, f). Therefore, biases in the eastern and western regions may cancel each other to some extent.

5.4. AMOC and MHT uncertainties due to computational methodology

In the previous section we analyzed the sensitivity of the AMOC and MHT to strategies for different temporal and spatial sampling of the AX18 XBT transect. In this section, we investigate how methodological assumptions affect the AMOC and MHT estimated at 34°S. First, we will explore the impact of salinity and deep temperature inferences. Additionally, we optimize the choice of the reference level, and propose a method to estimate the barotropic velocities across the transect.

5.4.1. Salinity and deep temperature inferences

To study the impact of salinity and deep temperature inferences on the AMOC and MHT, we perform step changes in the model observational strategy. We compute Ψ_y and MHT using: i) the constructed annual T-S lookup table (Section 5.1) to estimate salinity profiles in the upper 800 m, ii) padding the model T-S monthly climatology in the deep ocean (> 800 m deep), and iii) using both the lookup table in the upper ocean and padding in the deeper ocean.

We compare the changes in the geostrophic components of AMOC strength and MHT using these approximations against those calculated using the full model output. The main variability of the AMOC and MHT follow closely the ones from the approximated fields (not shown). The analysis of the residuals relative to the estimates from the full model outputs (Figure 9) show that the T-S lookup approximation drives most of the residual AMOC changes (0.35 $\pm$ 2.8 Sv). In addition, the residuals from the T-S lookup approximation are subject to strong seasonality. Biases in AMOC strength can reach -1 Sv during austral winter and 1 Sv during summer. This seasonal bias is due to the fact that the T-S relationships are taken from an annual mean.

Deep ocean padding biases show only a small seasonality, and AMOC mean biases are small, with magnitude of -0.03 $\pm$ 2.4 Sv. For the MHT, performing either padding or TS lookup approximations produce residual changes of -0.02 $\pm$ 0.13 PW and 0.04 $\pm$ 0.17 PW, respectively. These RMS errors calculated here are close to the value of $\pm$ 0.15 PW estimated for these approximations using the cumulative transport of the WOCE A10 section considered in *Baringer and Garzoli* [2007]. The results of our analysis using a six-year timeseries show that although the errors produced by salinity and deep temperature approximations are similar in value, the seasonal amplitude of the MHT and AMOC residuals using the TS lookup table is the largest (right panels in Figures 9a and 9b). Although these are conservative estimates, given that the model climatology represents well the variability below the surface, the errors caused by deep T-S padding are small in comparison to the other sources. Thus deployment of a whole water column CTD is not essential for a strong reduction of errors in the AX18 XBT transect.

5.4.2. Reference level for absolute geostrophic velocities

The barotropic mode accounts for most of the bias of the overturning circulation contribution [*Baehr et al.*, 2004]. As indicated from the model output (Figure 10), variations in bottom topography are the main driver of strong bottom velocities, which increases the barotropic contribution and its potential biases as well. Zonal sections, where boundaries are steeper and more similar to a vertical wall, can reduce the effect of the barotropic contribution [*Rayner et al.*, 2011]. At 34°S, where there are strong bottom velocities, large biases in the barotropic component could be introduced by assuming an inaccurate reference velocity. Here we perform four experiments to estimate the sensitivity of the barotropic AMOC (Ψ_{bar}) to the velocity ot the reference level. Similar to observational studies, we use in all experiments the reference depth at the $\sigma_2 = 37.09$. Since the velocity at the depth of $\sigma_2 = 37.09$ is below 3000 m, it is not well constrained by observations. Therefore we perform the following experiments: a) with zero reference velocity, b) with climatological reference velocity at the western boundary, c) with climatological reference velocity at the eastern boundary, and d) with climatological velocity at both western and eastern boundaries. Figure 11 shows the evolution and the time mean barotropic streamfunction (left and right panels, respectively), for the experiments (a–d).

The minimum of barotropic streamfunction, which characterizes its strength, is located between 2 and 3 km deep. Using model velocities, the mean Ψ_{bar} strength is estimated as -16.3 Sv. When zero reference velocity is assumed, a much weaker Ψ_{bar} strength value is estimated (Ψ_{bar} = -10.5 Sv; Figure 11a), or a mean bias of 5.7 $\pm$ 4.4 Sv. Because the barotropic streamfunction is the main balance of the vertical shear component in the model (Figure 3), a weaker Ψ_{bar} acts to increase the MHT by 0.17 $\pm$ 0.16. Adding a climatological reference velocity in the boundaries reduces the uncertainties in the barotropic mode. The derived Ψ_{bar} strength estimates using climatological reference velocities in the boundaries produce positive biases of 4.0 $\pm$ 4.5 Sv (0.06 $\pm$ 0.16 PW) in the western boundary and 2.0 $\pm$ 4.3 Sv (0.10 $\pm$ 0.14 PW) in the eastern side of the basin (Figures 11b and 11c, respectively). Therefore, the eastern boundary velocity information reduces uncertainties more than in the western boundary. When both eastern and western reference velocities are added (Figure 11d), the mean Ψ_{bar} = -16.0 Sv, and the Ψ_{bar} strength is correctly measured at value of 0.3 $\pm$ 4.4 Sv (-0.02 $\pm$ 0.14 PW). Further adding reference velocity information in the interior does not improve these uncertainty values.

Therefore, we show here that the misrepresentation of the reference velocities in the geostrophic calculation yields the highest contribution to the uncertainties in the AMOC and MHT calculations. Knowledge of the reference level velocities at both the western and eastern boundaries is necessary for considerably reducing the mean bias in the barotropic mode. This can be achieved by using climatological values in the boundaries, and this information may be acquired from available Argo float climatologies [e.g., *Goes et al.*, 2013b], for example. Although climatological reference velocities produce small mean biases in the AMOC and MHT estimates (0.3 Sv and -0.02 PW, respectively), there is still strong uncertainty in the lower frequency variability of the barotropic transport, given by their rmse, which are ± 4.4 Sv and ± 0.14 PW. To resolve the variability of the barotropic mode, additional available observations can be used. This question is addressed in the next section.

5.4.3. Alternative barotropic velocity estimation using altimetry and hydrography

In order to optimize the information necessary to monitor the AMOC at 34°S, several additional observations could be used to complement the AX18 XBT transect measurements. Some complimentary observations are already in place, such as the satellite wind stress measurements used to estimate the Ekman transport.

A topic of current research in the AMOC decomposition is the estimation of the barotropic mode. Using a reference level near the bottom of the ocean cannot capture interannual or longer variability due to the presence of deep flows, since in this work climatology is assumed below 800 m. Bottom pressure (P_{bot}) recorders are a useful platform to compute the time varying reference level for the meridional geostrophic velocity, and, therefore, estimate the non-steric component of the sea level height (SLH). Such a platform requires further investment in an array across the basin, and efforts are underway [*Perez et al.*, 2011; *Meinen et al.*, 2012]. Some recent studies use a blend of altimetry and Argo parking velocity as the reference level or level of known motion to infer absolute geostrophic velocities [*Willis and Fu*, 2008; *Mielke et al.*, 2013; *Goes et al.*, 2013b]. However, because a large number of Argo floats is necessary to produce a reliable estimate, seasonal averages are generally used in an Argo-based reference level. We showed in the previous section that a climatological assumption of the reference velocity in the eastern and western boundaries can reduce the AMOC mean bias considerably. Here we test another method for measuring the barotropic flow by using SLH derived from satellite altimetry in conjunction with hydrographic data. Altimetry captures both steric and non-steric components, whose contributions are variable among different regions of the ocean [*Guinehut et al.*, 2006]. The non-steric contribution generally increases toward higher latitudes due to weaker stratification and stronger Coriolis force. In some regions the non-steric contributions, such as the barotropic component, can account for more than 50% of the total sea level variability [*Shriver and Hurlburt*, 2000].

Using the hydrostatic relation, the total sea level can be accurately related to bottom and atmospheric (P_{atm}) pressure, plus the steric contribution [*Park and Watts*, 2005], respectively SLH $= (P_{bot} - P_{atm} - \rho_0 g H)/\rho_0 g$. In order to estimate the non-steric (P_{bot}) component of the sea level, we filter the steric contribution by calculating the residual between SLH and the dynamic height (DH) referenced at a certain level (SLH – DH). The barotropic velocities are calculated using geostrophy on this residual field, and the maximum barotropic streamfunction calculated from these velocities is then compared to the model barotropic streamfunction. Figure 12e shows how well this method represents the barotropic velocities across the basin at a certain instant of time.

We consider DH referenced at a certain depth, and estimate the optimal reference depth by varying the reference of DH from 300 m down to 3500 m deep (black curve with circles in Figure 12). According to our results, the structure of the variability of the barotropic velocities can be well captured by the non-steric sea level using this methodology. The strength of the barotropic AMOC show correlations above 0.5 irrespective of the reference level used in the DH estimation (Figure 12)b). High correlations (> 0.9) are found for a

DH reference level between 500 m and 1100 m. A low RMS region (< 5 Sv) is found for a reference level between 700-1100 m (Figure 12a), and overlaps with the high correlation region. The minimum RMS error of ~ 2.5 Sv is achieved when DH is referenced at 1000 m, where the bias in streamfunction is nearly zero (Figure 12)c), and standard deviation is close to a minimum (Figure 12)d). Below 1000 m, the uncertainties increase because assuming a deeper reference level for DH implies excluding the boundaries and regions where the topography is shallower than the reference depth. Finally, we quantify how much information is gained for the barotropic streamfunction estimation by using altimetry data. We compare the altimetry derived barotropic streamfunction with one calculated using the $\sigma_2 = 37.09$ as (i) a level of no motion or (ii) as the climatological reference velocity in the western and eastern boundaries (red and green curves in Figure 12, respectively). The correlation (0.74) and the standard deviation (4.4 Sv) (Figures 12b, d) are the same for the cases with a level of no motion or a climatological reference level at $\sigma_2 = 37.09$. Therefore, no gain exists in the variability of the barotropic mode by applying these two different assumptions. The bias, however, as we also found in Figure 11, decreases considerably, and is close to zero when applying a climatological reference level in the boundaries (Figure 12c). The bias reduction drives the reduction in RMS from 7.2 Sv to 4.4 Sv between these two cases. Using altimetry and DH referenced at 800 m, the maximum depth of an XBT profile, promotes a reduction of approximately 2 Sv in standard deviation and and increase of 0.15 in correlation towards the two approximations for the reference level at $\sigma_2 = 37.09$. Although we did not include measurement errors in these estimates, which would decrease the efficacy of the altimetry derived method, we also did not include any extrapolation for the boundaries, which would increase the efficacy of the method. Therefore, this result is a proof of concept that altimetry and XBT data are complementary platforms for the inference of the long term variability of the AMOC.

6. Conclusions

In this study we use a high resolution model assimilation product to assess the observational and computational uncertainties associated with estimating meridional transports using the data from the AX18 XBT transect along 34°S. We analyzed the AMOC and MHT in terms of their vertical shear, barotropic, and Ekman components. These terms are here used to reconstruct the AMOC and MHT. We show that this method is well suited for this type of work. In comparison to the AMOC calculated from the model velocities, the reconstructed AMOC streamfunction is able to represent the main model features, although the reconstruction cannot capture the high frequency reversals of the model AMOC and MHT during austral winter/spring. A key finding obtained here is that XBTs produce acceptable estimates of the AMOC and MHT variability, where the uncertainties obtained by the multiple sources of error are smaller than the signal of the time series variability. Therefore, the AX18 transect is a valuable and longstanding piece of a multiple platform monitoring system for the region, and efforts should be made to maintain and improve it. The results obtained here are summarized in Table 1, and the results of *Baringer and Garzoli* [2007] for MHT is added for comparision. As follows, we make recommendations for optimization of sampling and computational methodologies to improve estimates of the AMOC and meridional MHT:

- The effect of T-S padding of monthly climatology below 800 m on the AMOC (0.03 $\pm$ 2.4 Sv) and MHT (-0.02 $\pm$ 0.13) estimates is small in comparison to the other error sources. The effect of using salinity from the T-S lookup table in the upper 800 m is also small in comparison to the other components, and is about the same order as the deep ocean padding. However, seasonal biases in the annual climatology can produce AMOC monthly biases of as much as 1 Sv. Salinity from other measurements, such as Argo, can produce monthly climatologies of T-S relationships, which would in principle avoid these seasonal biases.

- Current quarterly sampling causes an average RMS error of $\pm$ 2.3 Sv and $\pm$ 0.23 PW in the climatological AMOC and MHT estimates, respectively. The optimal strategy to reduce this sampling error would be to carry out 12 transects per year, i.e. one per month, which is not feasible due to operational constraints. More realistically, it is desirable to conduct continuous realizations at current quarterly sampling for at least 15 years.

- Spatial subsampling in the interior produces small errors in the AMOC and MHT estimates compared to the errors produced at the boundaries. The current AX18 zonal sampling uses 25 km on the boundaries and 50 km in the interior of the basin. This current spatial sampling seems to be adequate to capture most of the variability of the meridional transports, although the western boundary resolution still shows large AMOC bias at the present sampling (1.7 $\pm$ 2.4 Sv). An increase in the western boundary sampling to 20 km would improve the accuracy of the current AMOC calculations by $\sim$ 1 Sv.

- As described in previous studies [e.g., *Kanzow et al.*, 2007, for 26.5°N], the barotropic mode is likely to be the most significant source of error in the AMOC and MHT calculations due to the extensive continental shelf along 34°S. Errors are on the order of 5.7 $\pm$ 4.4 Sv for the AMOC and 0.17 $\pm$ 0.16 PW for MHT if a level of no motion is used in $\sigma_2 = 37.09$ kgm^{-3}. Using at least climatological values as the reference velocities in both boundaries is necessary to reduce the AMOC and MHT mean biases to $\sim 0.3 \pm 4.4$ Sv and 0.02 ± 0.14 PW, respectively.

- The use of satellite altimetry observations in conjunction with hydrographic data is a good alternative for barotropic term estimation. We show that barotropic volume transport estimates using the non-steric component of altimetry can improve the RMS error by ~ 3 Sv in comparison to the commonly used level of no motion at σ_2 =37.09 kgm^{-3}.

Finally, this study assesses only one the part of the several platforms that are in place to monitor the variability of the AMOC and MHT in the South Atlantic, XBT and altimetry data. The utility of the other operational platforms, such as moorings and Argo data, has been demonstrated in various other studies [*Dong et al.*, 2011b; *Perez et al.*, 2011]. An analysis that includes a blend of several platforms is still necessary to evaluate the optimal observational system for the region.

Acknowledgments. The data used in this study are available in the following websites: the model assimilation runs at www.hycom.org, WOA05 temperature data at www.nodc.noaa.gov/OC5/WOA05/woa05data.html, AX18 transect data at www.aoml.noaa.gov/phod/hdenxbt/ax_home.php?ax=18, and SLA data at www.aviso.com. The authors want to thank Joe Metzger for providing the GLBa0.08/74.2 simulation output, Molly Baringer for scientific discussions, Johanna Baher for help with geostrophic calculations, and the ship companies Evergeen Lines, CMA CGM Lines, Hamburg Sud, Monte Azul, and MOL lines for carrying out the AX18 cruises as part of the Ships of Opportunity project. This research was accomplished under the auspices of the Cooperative Institute for Marine and Atmospheric Studies (CIMAS), a cooperative institute of the University of Miami and the National Oceanic and Atmospheric Administration, cooperative agreement #NA17RJ1226, and was partly funded by the NOAA Climate Program Office.

References

Baehr, J., J. Hirschi, J.-O. Beismann, and J. Marotzke (2004), Monitoring the meridional overturning circulation in the North Atlantic: A model-based array design study, *J. Mar. Res.*, *62*(3), 283–312, doi:10.1357/0022240041446191.

Baehr, J., D. McInerney, K. Keller, and J. Marotzke (2008), Optimization of an observing system design for the North Atlantic meridional overturning circulation, *J. Atmosph. Ocean. Tech.*, *25*(4), 625–634, doi:10.1175/2007JTECHO535.1.

Baringer, M., and S. Garzoli (2007), Meridional heat transport determined with expendable bathythermographs, Part I: Error estimates from model and hydrographic data, *Deep-Sea Res. I*, *54*(8), 1390–1401, doi:10.1016/j.dsr.2007.03.011.

Beal, L. M., W. P. M. D. Ruijter, A. Biastoch, R. Zahn, and S. 136 (2011), On the role of the Agulhas system in ocean circulation and climate, *Nature*, *472*(7344), 429–436, doi:10.1038/nature09983.

Biastoch, A., C. W. Böning, F. U. Schwarzkopf, and J. R. E. Lutjeharms (2009), Increase in Agulhas leakage due to poleward shift in the southern hemisphere westerlies, *Nature*, *462*, 495–498, doi:10.1038/nature08519.

Bryden, H. L., H. R. Longworth, and S. A. Cunningham (2005), Slowing of the Atlantic meridional overturning circulation at 25°N, *Nature*, *438*, 655–657, doi:10.1038/nature04385.

Chassignet, E., H. Hurlburt, E. Metzger, O. Smedstad, J. Cummings, G. Halliwell, R. Bleck, R. Baraille, A. Wallcraft, C. Lozano, H. Tolman, A. Srinivasan, S. Hankin, P. Cornillon, R. Weisberg, A. Barth, R. He, F. Werner, and J. Wilkin (2009), U.S. GODAE: Global ocean prediction with the hybrid coordinate ocean model (HYCOM), *Oceanography*, *22*(2), 64–75, doi:10.5670/oceanog.2009.39.

Cummings, J. A. (2005), Operational multivariate ocean data assimilation, *Quart. J. Royal Met. Soc., Part C*, *131*(613), 3583–3604, doi:10.1256/qj.05.105.

Dong, B.-W., and R. T. Sutton (2007), Enhancement of El Nino-Southern Oscillation ENSO variability by a weakened Atlantic thermohaline circulation in a coupled GCM, *J. Clim.*, *20*, 4920–4939, doi:10.1016/j.dsr2.2010.10.069.

Dong, S., S. L. Garzoli, M. O. Baringer, C. S. Meinen, and G. J. Goni (2009), Interannual variations in the Atlantic meridional overturning circulation and its relationship with the net northward heat transport in the South Atlantic, *Geophys. Res. Lett.*, *36*, L20,606, doi:10.1029/2009GL039356.

Dong, S., S. Garzoli, and M. Baringer (2011a), The role of interocean exchanges on decadal variations of the meridional heat transport in the South Atlantic, *J. Phys. Oceanogr.*, *41*, 1498–1511, doi:10.1175/2011JPO4549.1.

Dong, S., M. Baringer, G. Goni, and S. Garzoli (2011b), Importance of the assimilation of Argo float measurements on the meridional overturning circulation in the South Atlantic, *Geophys. Res. Lett.*, *38*, L18,603, doi:10.1029/2011GL048982.

Donners, J., and S. S. Drijfhout (2004), The lagrangian view of South Atlantic interocean exchange in a global ocean model compared with inverse model results, *J. Phys. Oceanogr.*, *34*, 1019–1035, doi:10.1175/1520-0485(2004)034<1019:TLVOSA>2.0.CO;2.

Ducet, N., P.-Y. L. Traon, and G. Reverdin (2000), Global high-resolution mapping of ocean circulation from Topex/Poseidon and ERS-1 and -2, *J. Geophys. Res.*, *105 (C8)*, 19,477–19,498, doi:10.1029/2000JC900063.

Enfield, D. B., A. M. Mestas-Nuez, and P. J. Trimble (2001), The Atlantic Multidecadal Oscillation and its relation to rainfall and river flows in the continental U.S., *Geophysical Research Letters*, *28*(10), 2077–2080, doi:10.1029/2000GL012745.

Fox, D., W. J. Teague, C. N. Barron, M. R. Carnes, and C. M. Lee (2002), The modular ocean data assimilation system (MODAS), *J. Atmos. Ocean. Technol.*, *19*, 240–252, doi:10.1175/1520-0426(2002)019<0240:TMODAS>2.0.CO;2.

Ganachaud, A., and C. Wunsch (2003), Large scale ocean heat and freshwater transports during the World Ocean Circulation Experiment, *J. Climate*, *16*, 696–705, doi: 10.1175/1520-0442(2003)016<0696:LSOHAF>2.0.CO;2.

Garzoli, S. (1993), Geostrophic velocities and transport variability in the Brazil/Malvinas confluence, *Deep-Sea Res.*, *40*, 1379–1403, doi:10.1016/0967-0637(93)90118-M.

Garzoli, S., and M. Baringer (2007), Meridional heat transport determined with expendable bathythermographs. Part II: South Atlantic transport, *Deep-Sea Res. I*, *54*, 1402–1420, doi:10.1016/j.dsr.2007.04.013.

Garzoli, S., M. Baringer, S. Dong, R. Perez, and Q. Yao (2013), South Atlantic meridional fluxes, *Deep-Sea Res. I*, *71*, 21–32, doi:10.1016/j.dsr.2012.09.003.

Garzoli, S. L., and R. Matano (2011), The South Atlantic and the Atlantic meridional overturning circulation, *Deep-Sea Res. Part II*, *58*(17–18), 1837–1847, doi: 10.1016/j.dsr2.2010.10.063.

Goes, M., N. M. Urban, R. Tonkonojenkov, M. Haran, A. Schmittner, and K. Keller (2010), What is the skill of ocean tracers in reducing uncertainties about ocean diapycnal mixing and projections of the atlantic meridional overturning circulation?, *J. Geophys. Res.*, *115*, C12,006, doi:10.1029/2010JC006407.

Goes, M., G. Goni, and K. Keller (2013a), Reducing biases in XBT measurements by including discrete information from pressure switches, *J. Atmos. Oceanic Technol.*, *30*, 810–824, doi:10.1175/JTECH-D-12-00126.1.

Goes, M., G. Goni, V. Hormann, and R. Perez (2013b), Variability of the Atlantic off-equatorial eastward currents during 1993-2010 using a synthetic method, *J. Geophys. Res.-Oceans*, *118*(6), 3026 – 3045, doi:10.1002/jgrc.20186.

Goni, G., and I. Wainer (2001), Investigation of the Brazil Current front variability from altimeter data, *J. Geophys. Res.*, *106*, 31,117–31,128, doi:10.1029/2000JC000396.

Goni, G., S. Garzoli, A. Roubicek, D. Olson, and O. Brown (1997), Agulhas ring dynamics from TOPEX/POSEIDON satellite altimeter data, *J. Mar. Res.*, *55*(5), 861–883, doi:10.1357/0022240973224175.

Goni, G., F. Bringas, and P. D. Nezio (2011), Observed low frequency variability of the Brazil Current front, *J. Geophys. Res.*, *116*, C10,037, doi:10.1029/2011JC007198.

Gordon, A. (1986), Interocean exchange of thermocline water, *J. Geophys. Res.*, *91*, 5037–5046, doi:10.1029/JC091iC04p05037.

Griffies, S. M., M. J. Harrison, R. C. Pacanowski, and A. Rosati (2004), A technical guide to MOM4, GFDL Ocean Group, *Tech. Rep. 5*, NOAA/GFDL, Princeton, NJ.

Guinehut, S., P.-Y. L. Traon, and G. Larnicol (2006), What can we learn from global altimetry/hydrography comparisons?, *Geophys. Res. Lett.*, *33*, L10,604, doi:

10.1029/2005GL0255551.

Hall, M. M., and H. L. Bryden (1982), Direct estimates and mechanisms of ocean heat transport, *Deep-Sea Res.*, *29*(3), 339–359, doi:10.1016/0198-0149(82)90099-1.

Hatun, H., A.-B. Sandø, H. Drange, B. Hansen, and H. Valdimarsson (2005), Influence of the atlantic subpolar gyre on the thermohaline circulation, *Science*, *309*, 1841–1844, doi:10.1126/science.1114777.

Hawkings, E., R. S. Smith, L. C. Allison, J. M. Gregory, T. J. Woollings, H. Pohlmann, and B. de Cuevas (2011), Bistability of the Atlantic overturning circulation in a global climate model and links to ocean freshwater transport, *Geophys Res Lett.*, *38*, L10,605, doi:10.1029/2011GL047208.

Hirschi, J., J. Baehr, J. Marotzke, J. Stark, S. Cunningham, and J.-O. Beismann (2003), A monitoring design for the Atlantic meridional overturning circulation, *Geophys. Res. Lett.*, *30*, 1413, doi:10.1029/2002GL016776.

Hu, A., G. A. Meehl, W. Han, and J. Yin (2011), Effect of the potential melting of the Greenland ice sheet on the meridional overturning circulation and global climate in the future, *Deep-Sea Res. II*, *58*, 1914–1926, doi:10.1029/2000GL012745.

Jayne, S. R., and J. Marotzke (2001), The dynamics of ocean heat transport variability, *Rev. Geophys.*, *39*, 385–411, doi:10.1029/2000RG000084.

Kanzow, T., S. A. Cunningham, D. Rayner, J. J.-M. Hirschi, W. E. Johns, M. O. Baringer, H. L. Bryden, L. M. Beal, C. S. Meinen, and J. Marotzke (2007), Observed flow compensation associated with the MOC at 26.5 degrees N in the Atlantic, *Science*, *317*(5840), 938–941, doi:10.1126/science.1141293.

Lee, T., and J. Marotzke (1998), Seasonal cycles of meridional overturning and heat transport of the Indian Ocean, *J. Phys. Oceanogr.*, *28*, 923–943, doi:10.1175/1520-0485(1998)028<0923:SCOMOA>2.0.CO;2.

Lentini, C., G. Goni, and D. Olson (2006), Investigation of Brazil Current rings in the confluence region, *J. Geophys. Res.*, *111*(C06013), doi:10.1029/2005JC002988.

Levermann, A., A. Griesel, M. Hofmann, M. Montoya, and S. Rahmstorf (2005), Dynamic sea level changes following changes in the thermohaline circulation, *Climate Dyn.*, *24*, 347–354, doi:10.1007/s00382-004-0505-y.

Locarnini, R. A., A. V. Mishonov, J. I. Antonov, T. P. Boyer, and H. E. Garcia (2006), World Ocean Atlas 2005, *Tech. Rep. V. 1: Temperature*, NOAA Atlas NESDIS 61, U.S. Government Printing Office, Washington, D.C.

Lohmann, K., H. Drange, and M. Bentsen (2009), A possible mechanism for the strong weakening of the north atlantic subpolar gyre in the mid-1990s, *Geophys. Res. Lett.*, *36*, L15,602, doi:1029/2009GL039166.

Marshall, J., and F. Schott (1999), Open-ocean convection: Observations, theory and models, *Rev. Geophys.*, *37*, 1–64, doi:10.1029/98RG02739.

Meinen, C. S., A. R. Piola, R. C. Perez, and S. L. Garzoli (2012), Deep Western Boundary Current transport variability in the South Atlantic: preliminary results from a pilot array at 34.5° S, *Ocean Sci. Discuss.*, *9*, 977–1008, doi:10.5194/osd-9-977-2012.

Mello, R. L., A. C. N. Freitas, L. Russo, J. F. Oliveira, C. A. S. Tanajura, and J. B. R. Alvarenga (2013), Ocean forecasts in the southwestern Atlantic: Impact of different sources of sea surface height in data assimilation, *Rev. Bras. de Geoísica*, *31(2)*, 243–255.

Mielke, C., E. Frajka-Williams, and J. Baehr (2013), Observed and simulated variability of the AMOC at 26°N and 41°N, *Geophys. Res. Lett.*, *40*(6), 1159–1164, doi:10.1002/grl.50233.

Montgomery, R. B. (1974), Comments on Seasonal variability of the Florida current, by Niiler and Richardson, *J. Mar. Res.*, *32*, 533–535.

Park, J.-H., and D. R. Watts (2005), Response of the southwestern Japan/East Sea to the atmospheric pressure, *Deep-Sea Res. II*, *52*, 1671–1683, doi:10.1016/j.dsr2.2003.08.007.

Perez, R. C., S. L. Garzoli, C. Meinen, and R. P. Matano (2011), Geostrophic velocity measurement techniques for the meridional overturning circulation and meridional heat transport in the South Atlantic, *J. Atmos. and Ocean. Tech.*, *28*(11), 1504–1521, doi:10.1175/JTECH-D-11-00058.1.

Pond, S., and G. Pickard (1983), *Introductory Dynamical Oceanography*, Pergamon international library of science, technology, engineering and social studies, Butterworth-Heinemann.

Rahmstorf, S. (1996), On the freshwater forcing and transport of the Atlantic thermohaline circulation, *Clim. Dyn.*, *12*, 799–811, doi:10.1007/s003820050144.

Rayner, D., J. J.-M. Hirschi, T. Kanzow, W. E. Johns, P. G. Wright, E. Frajka-Williams, H. L. Bryden, C. S. Meinen, M. O. Baringer, J. Marotzke, L. M. Beal, and S. A. Cunningham (2011), Monitoring the Atlantic meridional overturning circulation, *Deep-Sea Res. II*, *58*(17–18), 1744–1753, doi:10.1016/j.dsr2.2010.10.056.

Richardson, P., and S. Garzoli (2003), Characteristics of intermediate water flow in the Benguela Current as measured with RAFOS floats, *Deep-Sea Res.*, *50*, 87–118, doi:10.1016/S0967-0645(02)00380-6.

Sabine, C., R. Feely, N. Gruber, R. Key, K. Lee, J. Bullister, R. Wanninkhof, C. Wong, D. Wallace, B. Tilbrook, et al. (2004), The oceanic sink for anthropogenic CO2, *Science*, *305*, 367–371, doi:10.1126/science.1097403.

Shriver, J. F., and H. E. Hurlburt (2000), The effect of upper ocean eddies on the non-steric contribution to the barotropic mode, *Geophys. Res. Lett.*, *27*, 2713–2716, doi:10.1029/1999GL011105.

Sime, L. C., D. P. Stevens, K. J. Heywood, and K. I. Oliver (2006), A decomposition of the Atlantic meridional overturning, *J. Phys. Oceanogr.*, *36*(12), 2253–2270, doi:10.1175/JPO2974.1.

Stramma, L., and M. England (1999), On the water masses and mean circulation of the South Atlantic Ocean, *J. Geophys. Res.*, *104*((C9)), 20,863–20,883, doi:10.1029/1999JC900139.

Sutton, R. T., and D. L. R. Hodson (2005), Atlantic Ocean forcing of North American and European summer climate, *Science*, *309*, 115–118, doi:10.1126/science.1109496.

Thacker, W. C. (2008), Estimating salinity between 25° and 45°S in the Atlantic ocean using local regression, *J. Atmos. Ocean. Tech.*, *25*, 114–130, doi:10.1175/2007JTECHO530.1.

Timmermann, A., Y. Okumura, S.-I. An, A. Clement, B. Dong, E. Guilyardi, A. Hu, J. H. Jungclaus, M. Renold, T. F. Stocker, R. J. Stouffer, R. Sutton, S.-P. Xie, and J. Yin (2007), The influence of a weakening of the Atlantic meridional overturning circulation on ENSO, *J. Climate*, *20*, 4899–4919, doi:10.1175/JCLI4283.1.

Treguier, A. M., M. England, S. R. Rintoul, G. Madec, J. L. Sommer, and J.-M. Molines (2007), Southern Ocean overturning across streamlines in an eddying simulation of the

Antarctic circumpolar current, *Ocean Sci.*, *3*, 491–507, doi:10.5194/os-3-491-2007.

Wainer, I., P. Gent, and G. Goni (2000), Annual cycle of the Brazil-Malvinas confluence region in the National Center for Atmospheric Research climate system model, *J. Geophys. Res.*, *05*((C11)), 26,167–26,177, doi:10.1029/1999JC000134.

Weijer, W., W. P. M. D. Ruijter, H. A. Dijkstra, and P. J. van Leeuwen (1999), Impact of interbasin exchange on the Atlantic overturning circulation, *J. Phys. Oceanogr.*, *29*, 2266–2284.

Willis, J., and L.-L. Fu (2008), Combining altimeter and subsurface float data to estimate the time-averaged circulation in the upper ocean, *J. Geophys. Res.*, *113*(C12), 2156–2202, doi:10.1029/2007JC004690.

Woollings, T., J. M. Gregory, J. G. Pinto, M. Reyers, and D. J. Brayshaw (2012), Response of the North Atlantic storm track to climate change shaped by ocean-atmosphere coupling, *Nat. Geosci.*, *5*, 313–317, doi:10.1038/ngeo1438.

Zhang, R., and T. L. Delworth (2006), Impact of Atlantic multidecadal oscillations on India/Sahel rainfall and Atlantic hurricanes, *Geophys. Res. Lett.*, *33*, L17,712, doi:10.1029/2006GL026267.

Table 1. Bias $\pm$ RMS error of the AMOC (Sv) and MHT (PW) introduced by each source of error associated with the AX18 XBT transect observational assumptions estimated in the present study. Last column shows the error estimates of *Baringer and Garzoli* [2007], Table 3.

Source	AMOC (Sv)	Meridional Heat Transport (PW)	
	Present	Present	B&G
Upper ocean salinity	0.35 $\pm$ 2.8	0.04 $\pm$ 0.17	0.03
Deep climatology below 800 m	-0.03 $\pm$ 2.4	-0.02 $\pm$ 0.13	0.15
Mass imbalance	0.9 $\pm$ 3.8	-0.02 $\pm$ 0.06	0.02
Non-synopticity	0.2 $\pm$ 4.1	0.01 $\pm$ 0.25	–
Quarterly sampling	$\pm$ 2.3	$\pm$ 0.23	–
Unresolved western shelf transport	-0.6 $\pm$ 0.8	10^{-8}	0.01
Unresolved eastern shelf transport	0.15 $\pm$ 0.4	10^{-8}	0.01
Western Horizontal resolution (25 km)	1.7 $\pm$ 2.4	0.03 $\pm$ 0.06	–
Eastern Horizontal resolution (25 km)	1.0 $\pm$ 1.4	-0.03 $\pm$ 0.04	–
Interior Horizontal resolution(50 km)	-0.1 $\pm$ 1.1	0.01 $\pm$ 0.06	–
Western Reference level	4.0 $\pm$ 4.5	0.06 $\pm$ 0.16	0.05
Eastern Reference level	2.0 $\pm$ 4.3	0.10 $\pm$ 0.14	0.05

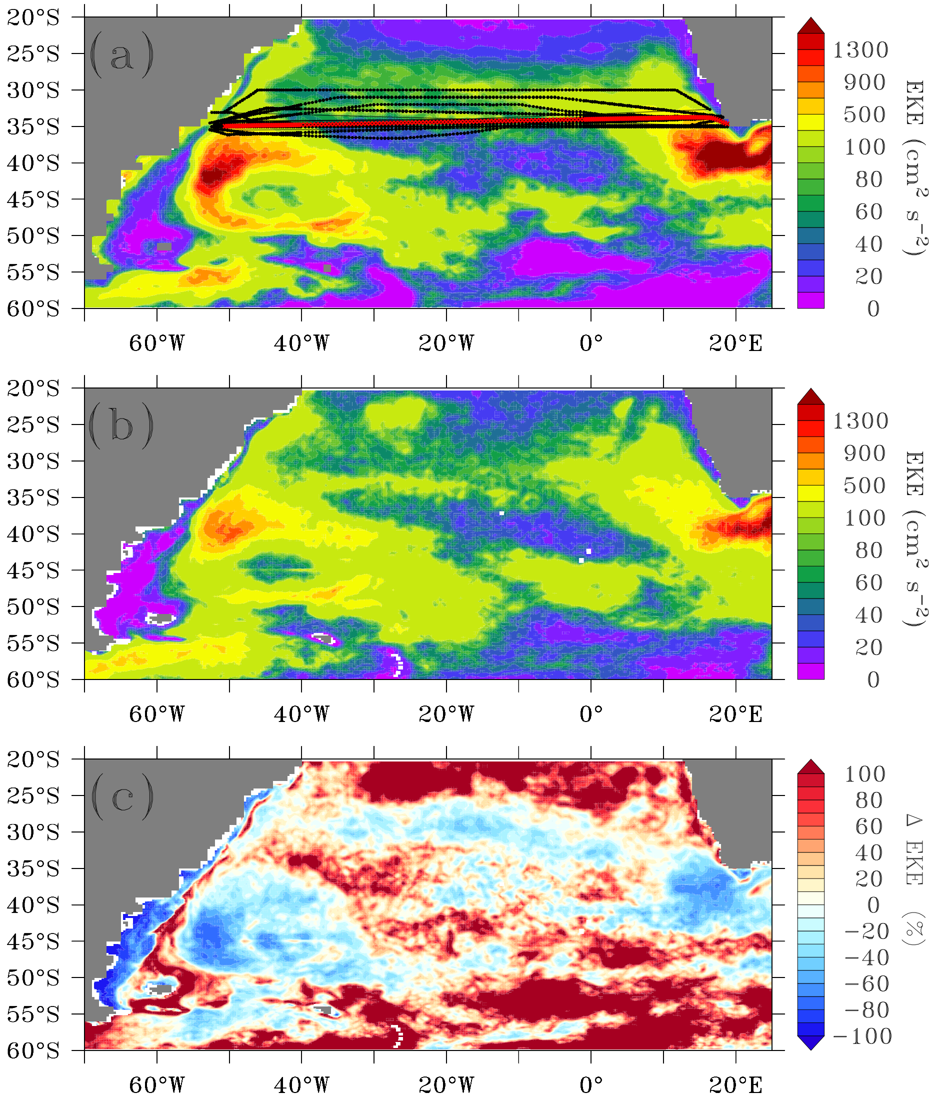

Figure 1. Eddy kinetic energy (cm^2 s^{-2}) calculated from sea level anomalies for the period between 2007 and 2013. (a) AVISO observations, (b) HYCOM model, and (c) HYCOM minus observations (in percentage changes). The black lines in Figure 1a are the locations of the 18 selected AX18 transects between 2002 and 2012, overlaid by the mean AX18 transect location in red.

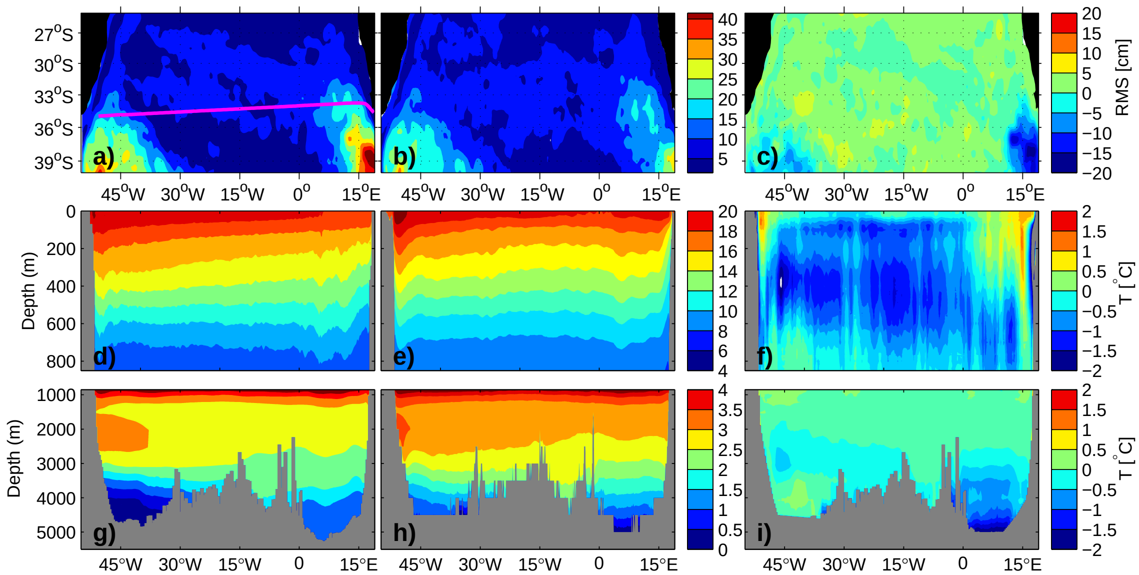

Figure 2. (a) – (c) Sea level anomaly (SLA) root-mean-square (RMS) contours (in cm) for: (a) AVISO overlaid by the mean AX18 transect (magenta line); (b) HYCOM/NCODA; (c) HYCOM/NCODA minus AVISO. (d)–(i): Mean temperature sections contours (in °C) for: (d, g) observations, with AX18 data for the upper 850 m (d) and WOA05 for 850 m to bottom (g); (e, h) HYCOM/NCODA model; (f, i) HYCOM/NCODA minus observations.

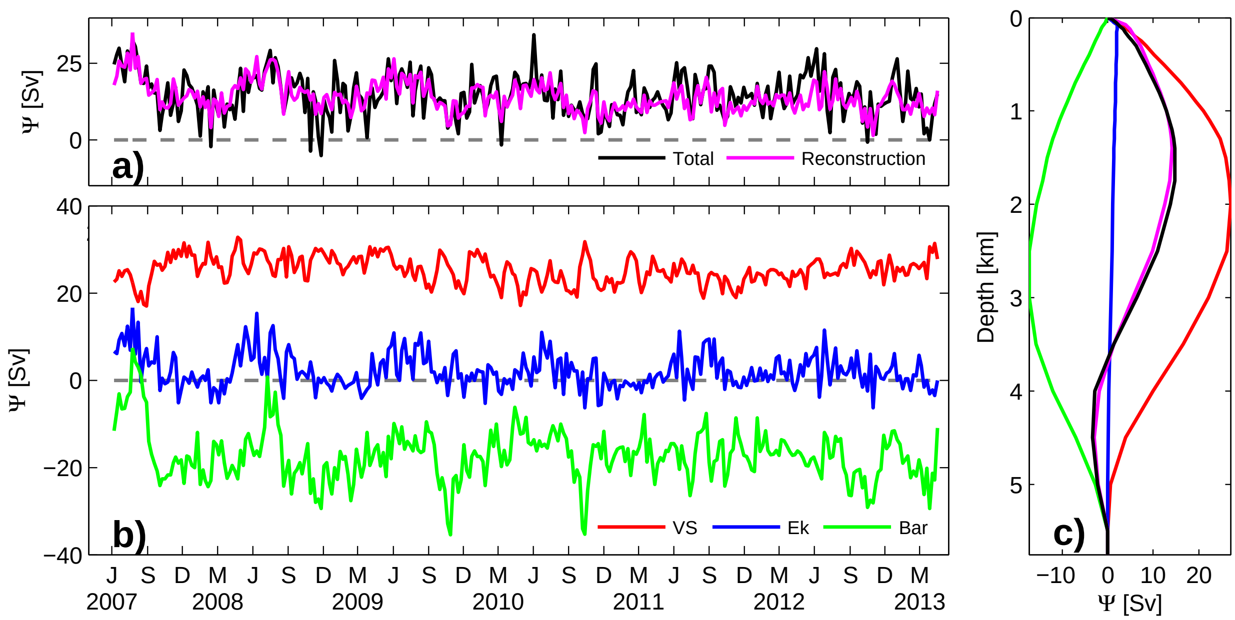

Figure 3. (a) Maximum volume transport streamfunction (AMOC) using model velocities (black) and the reconstruction (magenta). (b) AMOC decomposition into vertical shear (red), Ekman (blue), and barotropic (green) components. (c) Time mean meridional transport streamfunction for the model velocities (black), reconstruction (magenta), Ekman (blue), vertical shear (red) and barotropic (green).

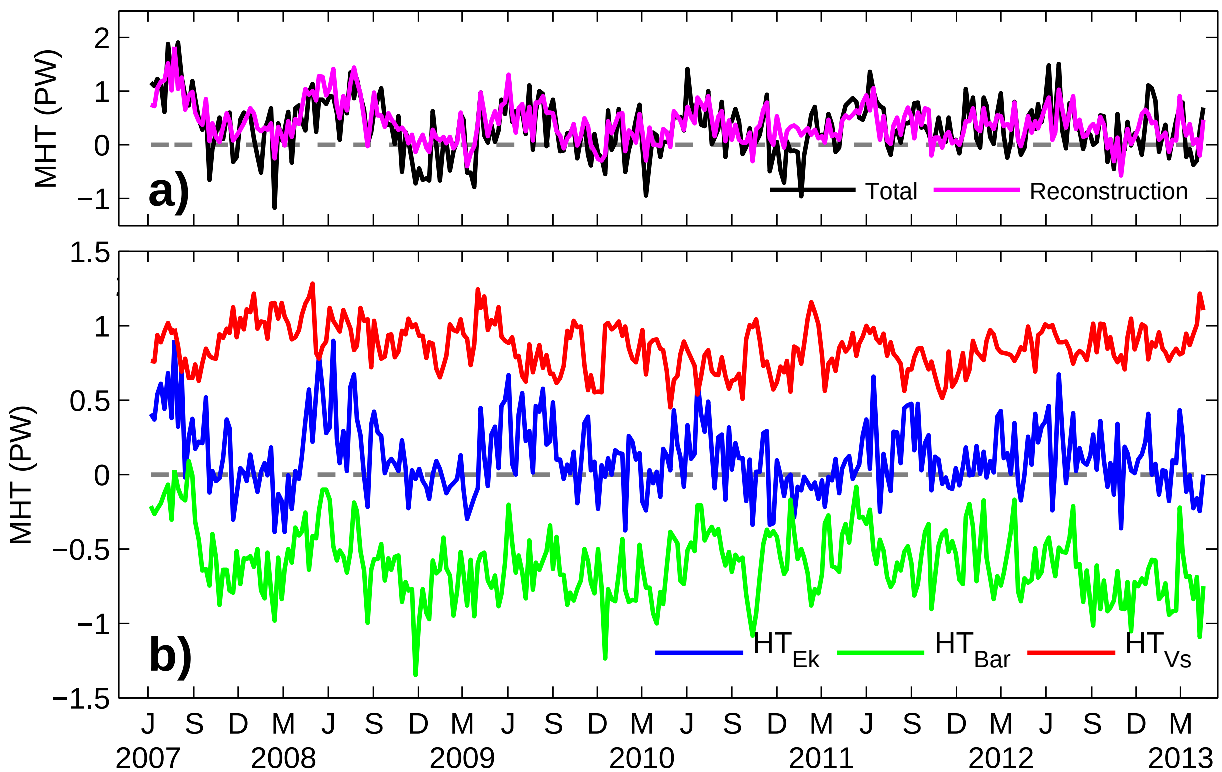

Figure 4. (a) Heat transport (MHT in PW) using model velocities (black) and reconstruction (magenta). (b) MHT decomposition into vertical shear (red), Ekman (blue), and barotropic (green) components.

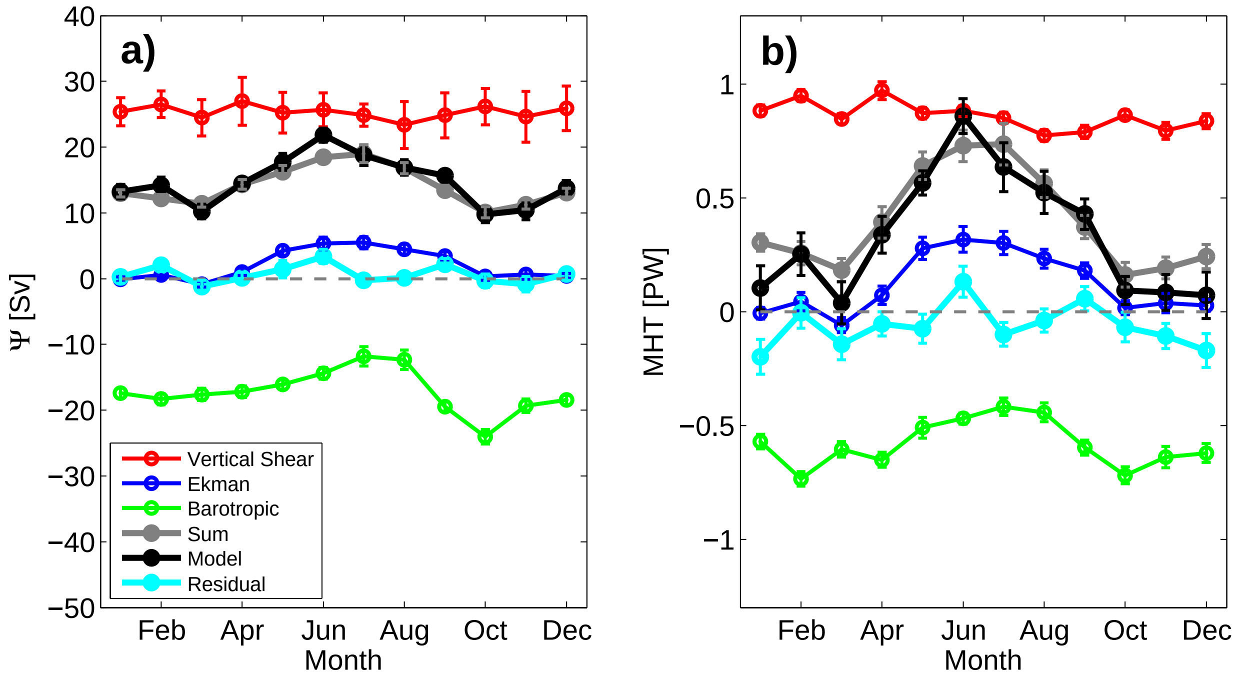

Figure 5. Monthly means of the (a) AMOC and (b) MHT components: vertical shear (red), Ekman (blue) and barotropic (green). The level of reference is assumed to be on the ocean bottom using the model bottom velocities as the reference. The sum of the transport components (gray) is comparable to the total transport from the original model velocities (black).

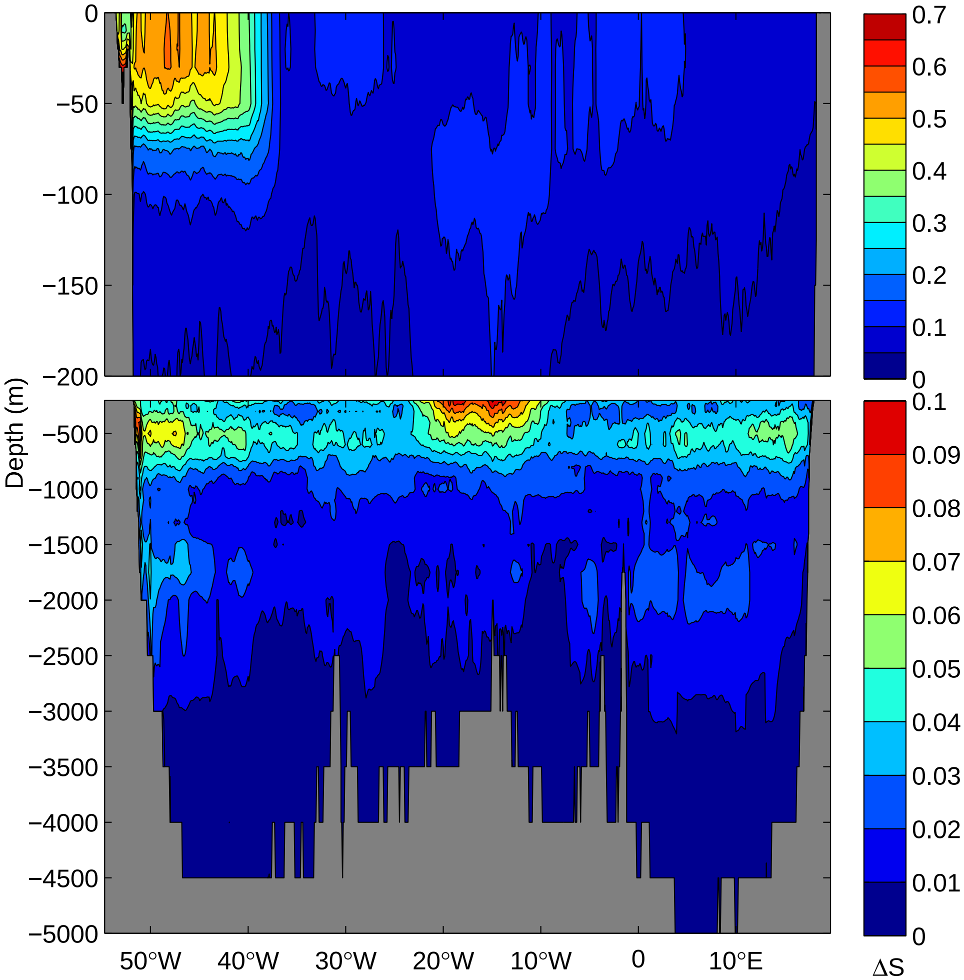

Figure 6. RMS error (psu) between the estimated salinity using climatological T-S relationships and the model salinity along the 34.5°S section.

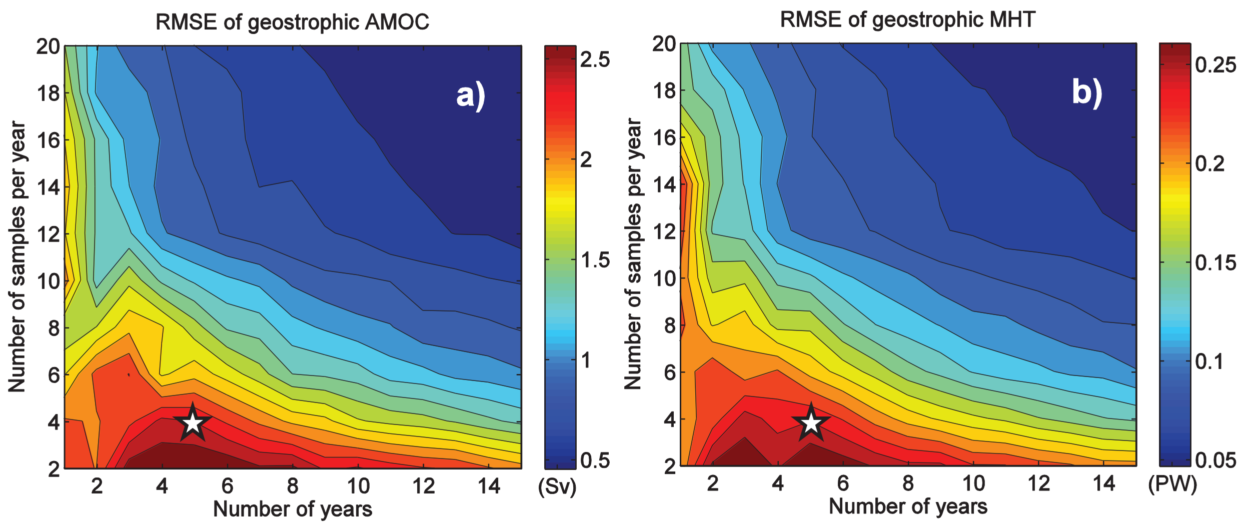

Figure 7. RMS error of geostrophic AMOC (a) and MHT (b) associated with different time samplings, i.e., the number of samples per year (y-axis) and the number of year (x-axis). The RMS error is calculated from the difference between the reconstructed time series using a different time sampling and the reconstructed time series using the original model sampling. The number of samples per year is randomly selected, and this process is realized 400 times to average the random realizations. The stars in (a) and (b) correspond to the current location of the AX18 sampling in the time sampling parameter space.

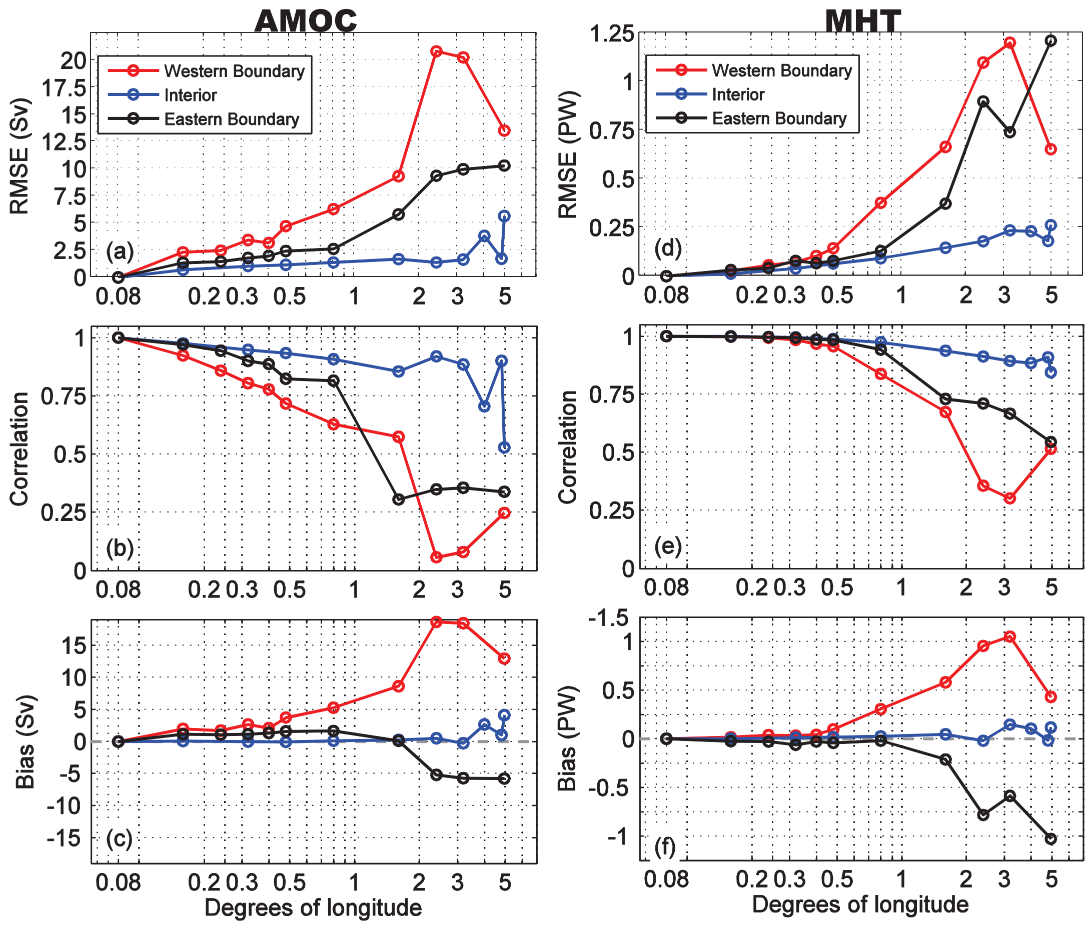

Figure 8. RMS error, correlation, and bias of the AMOC (a, b, c) and MHT (d, e, f) with respect to the simulated longitudinal resolution (in degrees) of the AX18 transect. The transect horizontal resolution varies individually for three regions, western boundary (red), interior (blue) and eastern boundary (black). The x-axis is shown in logarithmic scale.

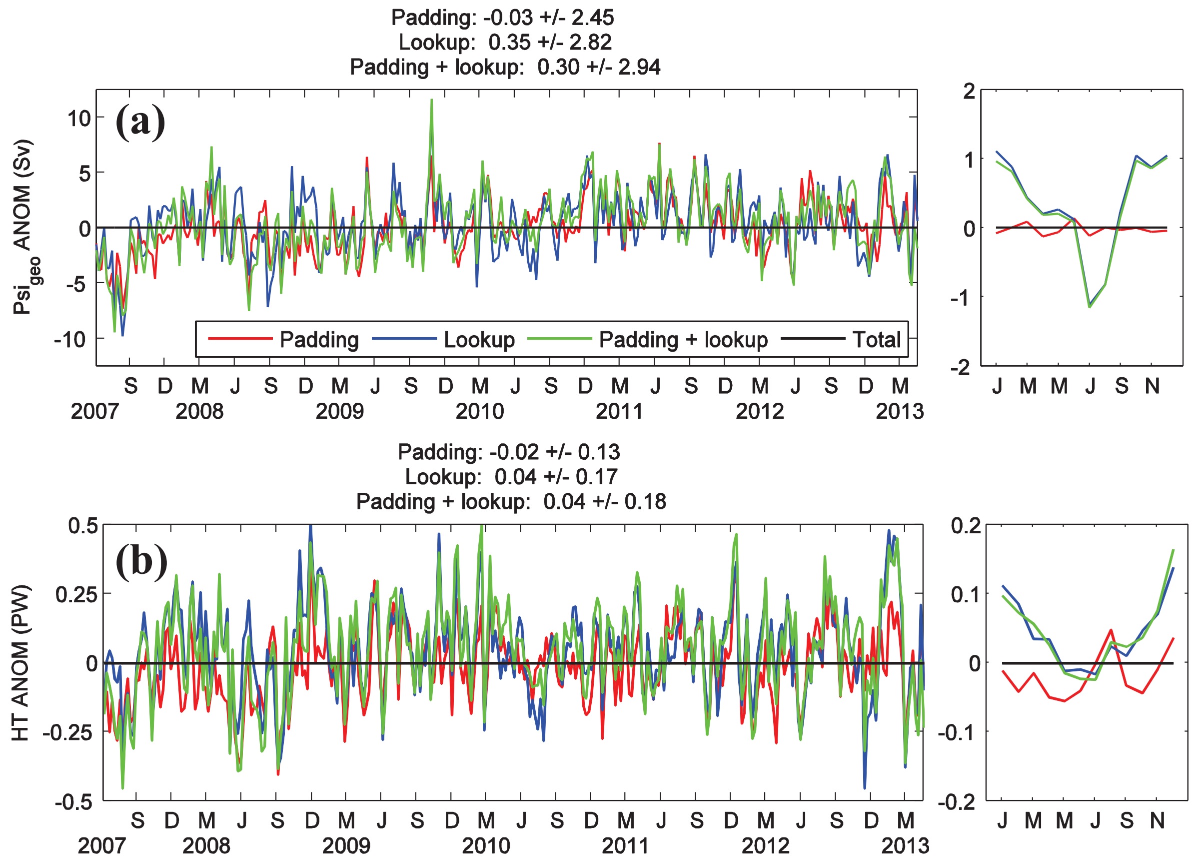

Figure 9. Anomalies relative to the total model field time series of (a) geostrophic AMOC and (b) MHT, and respective monthly averages (right panels). The total field anomalies are defined as having zero value (black), and the colored time series assume a bottom T-S climatology padding (red), salinity inference from lookup table in the top 800 m (blue), padding plus T-S lookup (green), and the total (black).

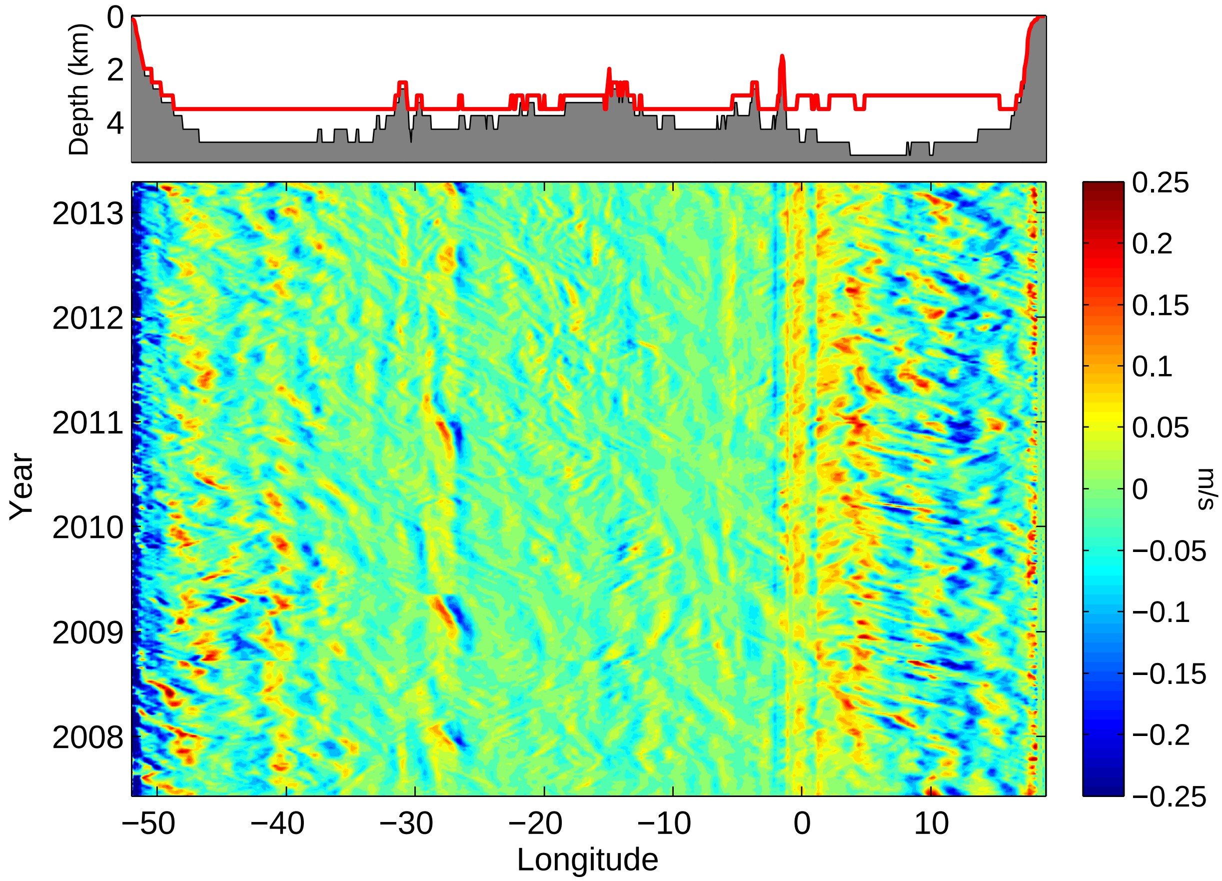

Figure 10. Barotropic velocities at 34.5°S estimated from the model velocities. The top panel shows the average depth of the $\sigma_2 = 37.9$ (red line) overlaid on model bathymetry

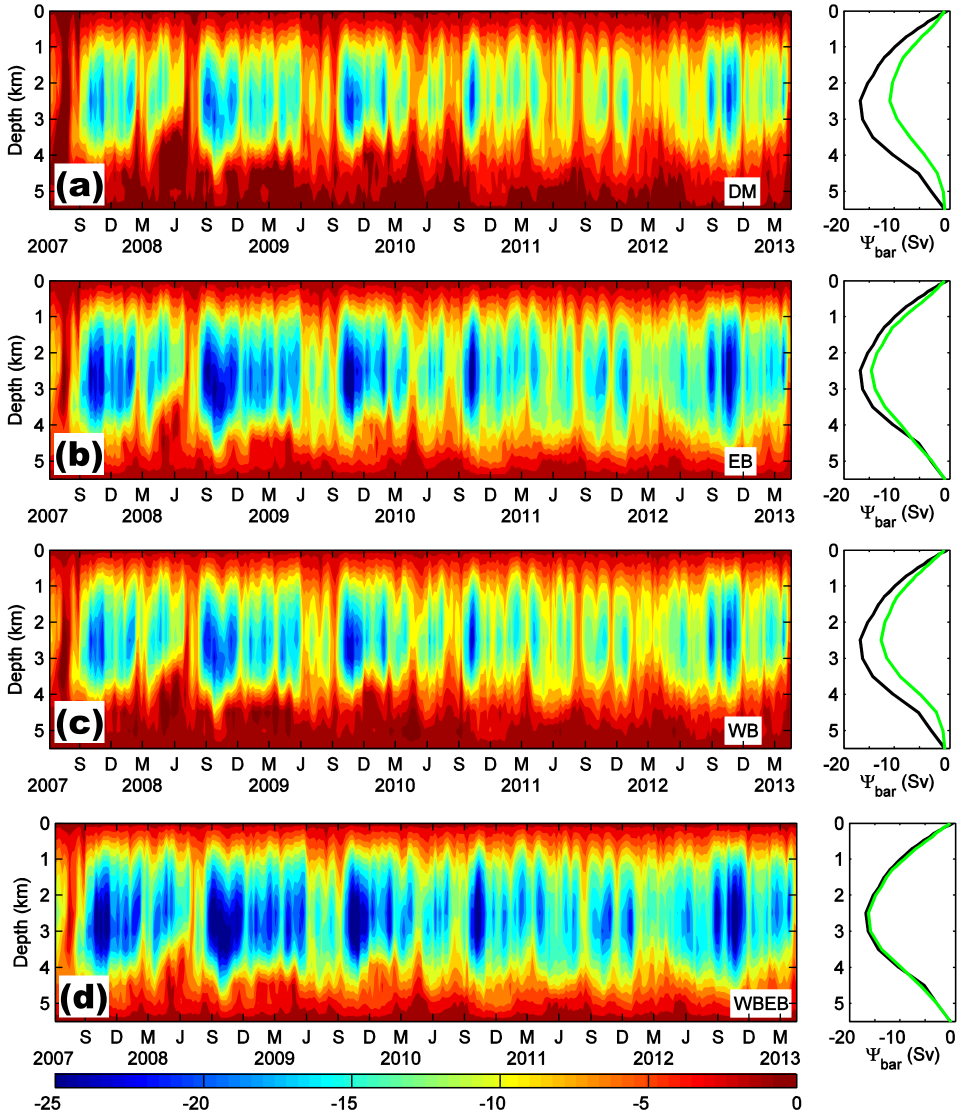

Figure 11. Changes in the barotropic streamfunction (Sv) due to the knowledge of a climatological reference velocity at $\sigma_2 = 37.09$. (a) Zero reference velocity, (b) eastern boundary, (c) western boundary, and (d) western plus eastern boundaries. Left panels: time evolution of the barotropic streamfunction. Right panels: green line is the time average of the barotropic streamfunction shown on the left panels, and black line is the time average of the original model barotropic streamfunction.

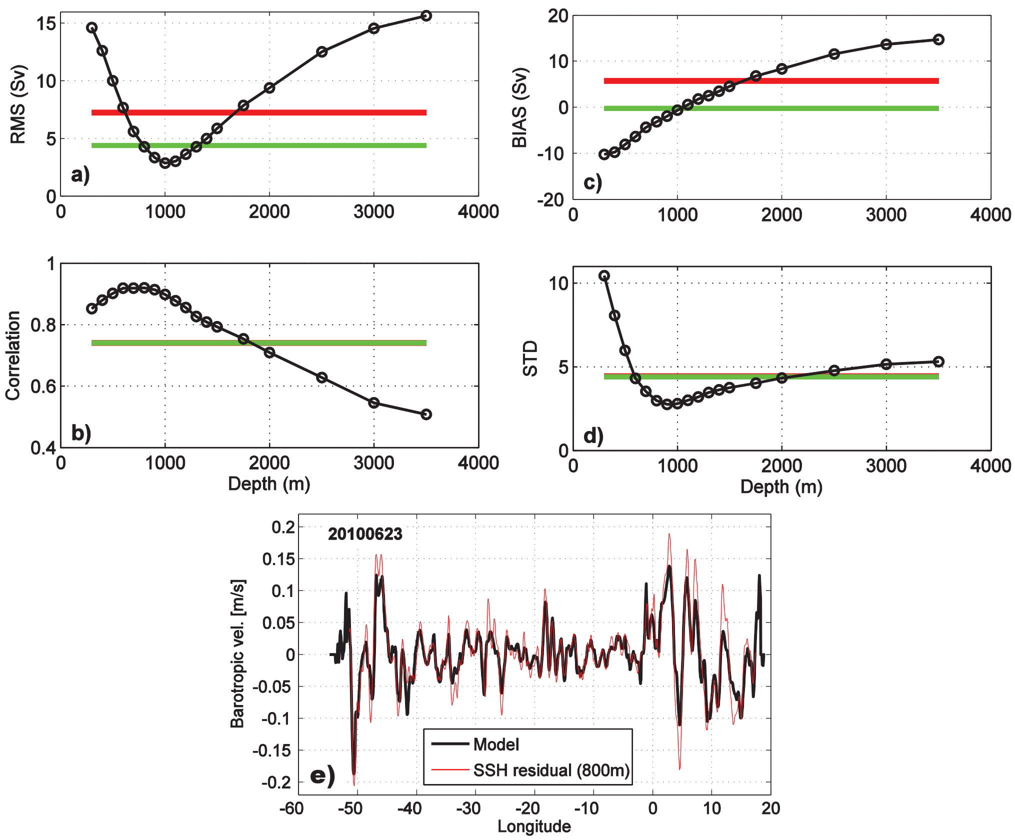

Figure 12. a) RMS error (Sv), (b) correlation, (c) bias (Sv) and (d) standard deviation (Sv) between the barotropic streamfunction strength for the barotropic velocities calculated from the SLH-DH residual with a variable reference level (x-axis) from 300 m to 3500 m depth (black line with open dots). The respective values of the barotropic streamfunction strength calculated using geostrophic velocities referenced to a level of no motion at $\sigma_2 = 37.09$ kg m^{-3} (red curve), and using the climatological model velocity values on the boundaries at $\sigma_2 = 37.09$ kg m^{-3} (green curve).(e) Comparison of a snapshot between the barotropic velocities (m/s) calculated from model velocities (black) and using the SSH-DH residual